Radiometric performance results of the *New Horizons' ALICE* UV imaging spectrograph

David C. Slater[a], Michael W. Davis[a], Catherine B. Olkin[b], John Scherrer[a], and S. Alan Stern[b]

[a]Southwest Research Institute, 6220 Culebra Rd., San Antonio, TX 78238
[b]Southwest Research Institute, 1050 Walnut St., Suite 400, Boulder, CO 80302

ABSTRACT

We describe the radiometric performance and calibration results of the *New Horizons' ALICE* flight model. This *ALICE* is a lightweight (4.4 kg), low-power (4.4 W), ultraviolet spectrograph based on the *ALICE* instrument now in flight aboard the European Space Agency's *Rosetta* spacecraft. Its primary job will be to detect a variety of important atomic and molecular species in Pluto's atmosphere, and to determine their relative abundances so that a complete picture of Pluto's atmospheric composition can be determined for the first time. *ALICE* will also be used to search for an atmosphere around Pluto's moon, Charon, as well as the Kuiper Belt Objects (KBOs) *New Horizons* hopes to fly by after Pluto-Charon. Detailed radiometric performance results of the *ALICE* flight model are presented and discussed.

Keywords: UV spectroscopy, New Horizons, Pluto, Charon, Kuiper Belt Objects, radiometric, calibration

1. INTRODUCTION

The New Horizons *ALICE* UV imaging spectrograph is a low-cost instrument designed to perform spectroscopic investigations of planetary atmospheres and surfaces at extreme (EUV) and far-ultraviolet (FUV) wavelengths between 520 and 1870 Å. *ALICE* is a direct derivative of the Pluto mission HIPPS UV spectrograph (HIPPS/UVSC) which scientists at Southwest Research Institute (SwRI) developed and breadboarded with funds from NASA, JPL, and SwRI[1]. The HIPPS/UVSC instrument was subsequently optimized for the European Space Agency's (ESA) *Rosetta* mission cometary science by increasing its sensitivity, instantaneous field-of-view (FOV), and wavelength coverage, and by adding a lightweight microprocessor. This instrument, *Rosetta-ALICE* (*R-ALICE*)[2], was successfully launched in March 2004 and is now en route on a 10-year mission to orbit about comet 67P/Churyumov-Gerasimenko. An improved derivative of *R-ALICE* was built and tested for the *New Horizons'* (NH) remote sensing suite. NH *ALICE* (also called *P-ALICE*) includes an airglow (AG) entrance aperture for airglow observations and a solar occultation channel (SOC) for direct solar observations at 30 AU. The SOC allows for solar occultation observations through Pluto's atmosphere during the NH flyby, and allows sensing for an atmosphere surrounding Charon and the targeted Kuiper Belt Object(s). The scientific objectives of the *P-ALICE* instrument aboard the New Horizons' mission to Pluto/Charon and the Kuiper Belt are given in Stern *et al.*[3].

2. INSTRUMENT DESCRIPTION

Figure 1 shows an opto-mechanical schematic of the interior of the *P-ALICE* instrument. A photograph of the exterior of the flight instrument is shown in Figure 2. Light can enter the telescope section through either a 40 x 40 mm^2 entrance aperture (i.e. the airglow channel) or a stopped-down 1-mm diameter entrance aperture and flat relay mirror (i.e. the SOC) and is collected and focused by an off-axis paraboloidal (OAP) primary mirror onto the spectrograph entrance slit. The OAP has a 120 mm focal length.

The entrance slit design, shown in Figure 3, is composed of two contiguous sections: i) the airglow slit with a FOV of 0.1° in the dispersion direction by 4° in the spatial direction; and ii) the SOC 2° x 2° square FOV located just above (and contiguous to) the airglow slit.

Light passing through the entrance slit falls onto a toroidal holographic diffraction grating with 1600 grooves/mm and a radius-of-curvature of 150 mm in the dispersion plane. The light is then dispersed onto a microchannel plate (MCP) detector that uses a double-delay line (DDL) readout scheme[4]. The 2-D (1024 x 32)-pixel format, MCP detector uses dual, side-by-side, solar-blind photocathodes: potassium bromide (KBr) covers the wavelength range of 520-1180 Å, and cesium iodide (CsI) covers the range 1250-1870 Å. A 70 Å gap exists between the two photocathodes where there is only bare MCP glass; this gap was designed to attenuate bright solar H I Ly-α emission at 1216 Å by a factor of ~10-30, in order to reduce the potential for detector saturation.

The detector's MCP configuration is a Z-stack that is cylindrically curved to match the 150-mm Rowland circle diameter to optimize spectral and spatial focus across the *P-ALICE* passband[5]. The detector electronics provide two stimulation pixels that can be turned on to check data throughput and acquisition modes without the need to apply high voltage to the MCP stack or to have light on the detector. The MCP pulse-height distribution (PHD) is output in the data stream and is accumulated into a 64-bin histogram that is embedded into the histogram images.

P-ALICE is controlled by a radiation-hardened version of the Intel 8051/8052 micro-controller, and utilizes lightweight, compact, surface mount electronics to support the science detector as well as the instrument support and interface electronics. The resulting design is highly systems-engineered to minimize mass and complexity, and enjoys strong parts-level heritage from the previous *R-ALICE* instrument[2]. A summary of the performance of *P-ALICE* is given in Table 1. Additional instrument design and functional details can be found in Stern *et al.* [3].

Table 1. *P-ALICE's* Characteristics, Spacecraft Resource Requirements, & Performance Summary

Bandpass:	520 – 1870 Å
Spectral Resolution:	~3-4 Å (point source; wavelength dependant)
	~10 Å (extended source)
Spatial Resolution:	0.05° x 0.6°
Active FOV	0.1° x 4.0° (airglow) + 2° x 2° (solar occultation)
Peak Effective Area:	0.2 to 0.3 cm^2 (1000-1100 Å)
Telescope/Spectrometer	Off-axis telescope, Rowland circle spectrograph
Detector Type	2-D Microchannel Plate w/ double-delay line readout
External Dimensions	44 x 16 x 12 cm^3
Mass/Power	4.4 kg/4.4 W

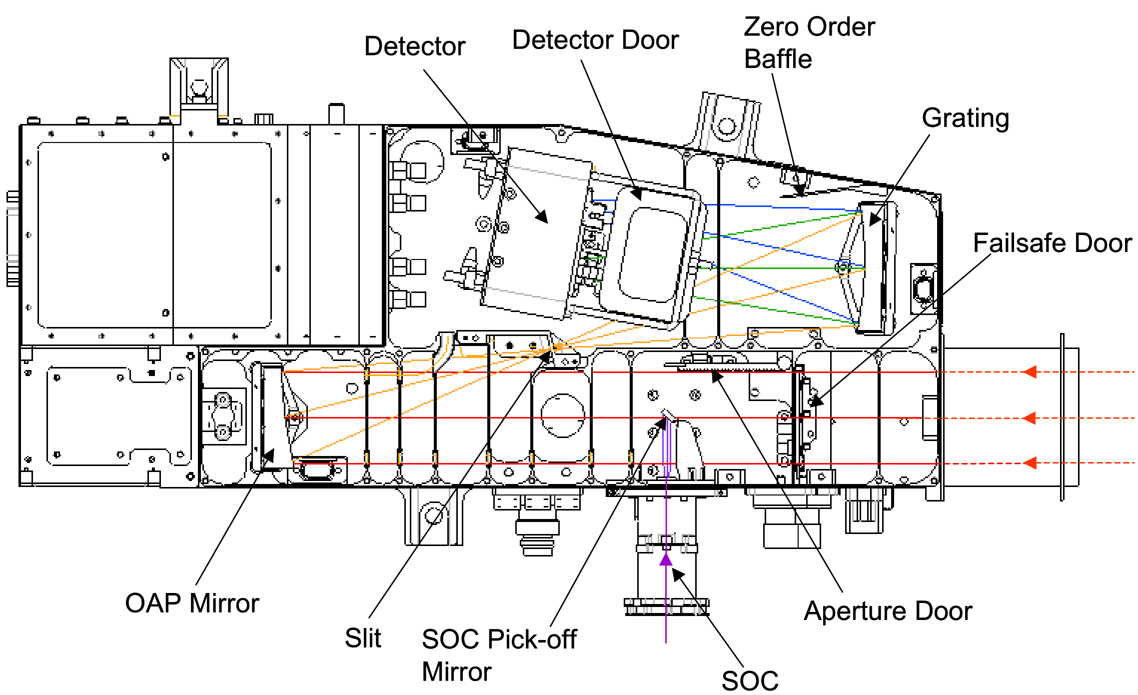

Figure 1. An opto-mechanical schematic of *P-ALICE* showing light rays traced through the main aperture door (airglow channel) and the solar occultation channel (SOC).

P-ALICE has two detector data collection modes described in detail below: i) image histogram mode and ii) pixel list mode. The *P-ALICE* flight software controls both of these modes.

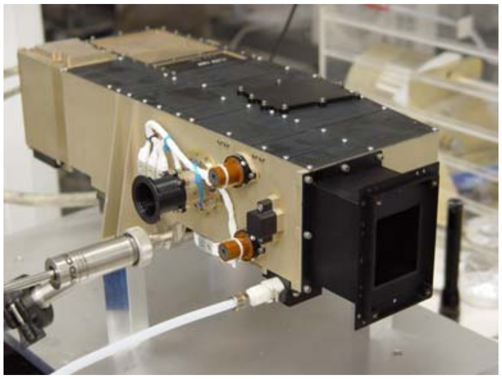

Figure 2. Photograph of the flight *P-ALICE* instrument prior to integration onto the NH spacecraft.

Image Histogram Mode. In image histogram mode, event data from the detector electronics representing (*x, y*)-pixel coordinates are passed to histogram memory in parallel form. The parallel data stream of *x* and *y* values is used as an address for a cell of two-bytes depth in the 1024 x 32 element histogram memory, and a read-increment-write operation on the cell contents is performed for each event. During a specified integration time, events are accumulated one at a time into their respective histogram array locations creating a 2-D image. At the conclusion of the integration period, the histogram memory can be manipulated to (a) extract up to eight separate windows in the array for downlink; (b) extract the entire array for downlink; or (c) extract and co-add rows/columns from up to eight separate windows (or the entire array) for downlink.

Pixel List Mode. Pixel list mode allows for the sequential collection of each (*x*, *y*)-event address into the histogram memory array. Periodically, at programmable rates not exceeding 256 Hz, a time word (a.k.a. "time hack") is inserted into the array to allow for "time-binning" of events. This mode can be used to either (a) lower the downlink bandwidth for data collection integrations with very low counting rates; or (b) for fast time-resolved acquisitions using relatively bright targets in the *P-ALICE* field-of-view. Two "ping-pong" memory buffers within the *P-ALICE* command-and-data-handling (C&DH) electronics allow contiguous pixel list exposures at detector count rates exceeding 50 kHz. This mode will be the primary data collection mode during the solar and stellar occultation observations of Pluto and Charon.

3. PRELIMINARY GROUND CALIBRATION RADIOMETRIC PERFORMANCE

At the completion of the *P-ALICE* instrument integration activities, *P-ALICE* underwent an environmental test program that included vibration, electromagnetic interference (EMI), and thermal-vacuum testing. Following these tests, radiometric characterization and absolute calibration of the instrument were performed in our UV calibration facility located in the SwRI Space Science and Engineering Division. The radiometric characterization tests included the following: detector dark count rate, wavelength calibration, spectral and spatial point source function (PSF) vs. wavelength, filled slit spectral resolution, and off-axis stray light attenuation. Finally, the absolute effective area was measured as a function of wavelength through both the AG and SOC channels.

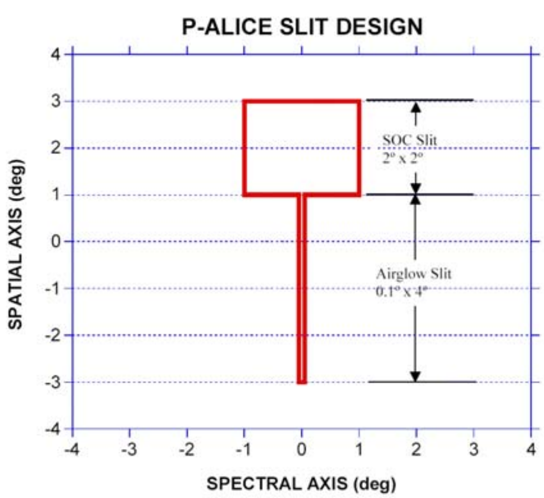

Figure 3. The *P-ALICE* entrance slit design. The narrow 0.1º x 4º slit is designated the "airglow" slit; the larger 2º x 2º opening above the airglow slit is the SOC slit. The airglow optical boresight is centered at (0º, 0º).

We present the preliminary results of these radiometric tests in the remainder of this paper.

The radiometric vacuum chamber used to test *P-ALICE* consists of a 4-inch diameter off-axis parabolic collimator mirror that is fed by a differentially-pumped hollow-cathode UV light source[6] and an Acton Research Corporation VM-502 vacuum monochromator. A variable slit and pinhole assembly at the output of the monochromator (and situated at the focus of the collimator mirror) allowed for point source illumination of the *P-ALICE* AG and SOC input apertures. *P-ALICE* was mounted to motorized translation and tip/tilt rotation stages within the vacuum chamber that allowed for instrument motion with respect to the collimated input beam. A set of NIST-calibrated photodiodes (one windowless and one silicon PN photodiode) and an AmpTek channeltron were used to measure the relative and absolute fluxes of the collimated beam for absolute effective area measurements. The chamber pressure during the radiometric calibration data runs were in the 5 x 10^{-7} to 5 x 10^{-6} Torr range. The higher-pressure periods were during operation of the hollow-cathode light source when gas was flowing through the light source.

3.1. Dark Count Rate

The detector dark count rate was measured via a set of pixel-list exposures that totaled 9.1 hours of accumulated exposure time. These datasets allowed us to examine both the temporal and spatial distribution of the dark noise and measure its rate. The time hack interval for these exposures was 0.512 s. Figure 4 shows the event rate as a function of time during one 1.4-hour exposure run. The average dark count rate over the 9.1-hour total exposure interval varied between 2.35 and 2.46 counts s^{-1} (0.29-0.31 count cm^{-2} s^{-1}) with Poissonian counting statistics ($\sigma \sim \pm$ 0.67 counts s^{-1} averaged over 5.12 second bins). This rate is well below the specified dark rate value of < 1 count cm^{-2} s^{-1}. Figure 5 shows the accumulated 9.1-hour dark exposure in 2-D histogram format. Figure 6 shows the row and column sums of the total dark exposure. The dark events are uniformly distributed over the entire array with three slightly more active dark regions at i) center right, ii) top center, and iii) bottom center (max rate ~3 x 10^{-4} counts s^{-1} $pixel^{-1}$). Event pileup at the left and right edges of the array, a characteristic of the DDL detector/electronics, is evident in Figures 5 and 6.

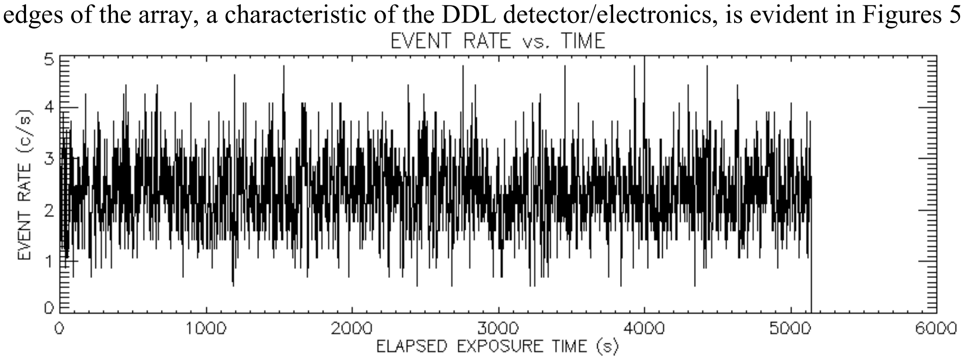

Figure 4. The total detector dark count rate as a function of time (smoothed over a 5.12 s period) during one set of dark cal pixel list exposures totaling ~1.4 hours. The average rate in this exposure was 2.37 ± 0.67 counts s^{-1}.

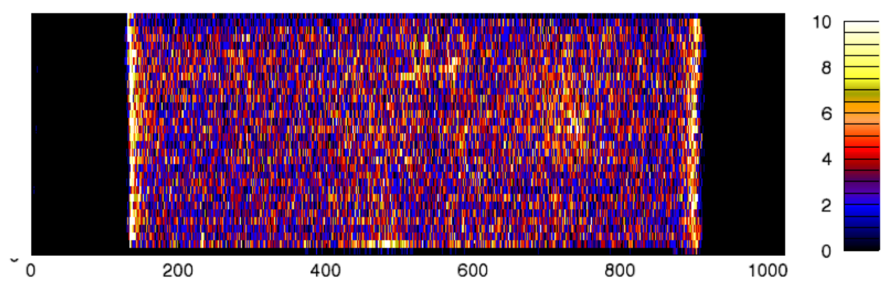

Figure 5. Image histogram of the total, 9.1 hour, accumulated dark count exposure. The horizontal axis is the spectral axis (780 active pixels); the vertical axis is the spatial axis (30 active pixels). The vertical color bar scale at right is in units of accumulated counts per pixel over the entire 9.1-hour exposure.

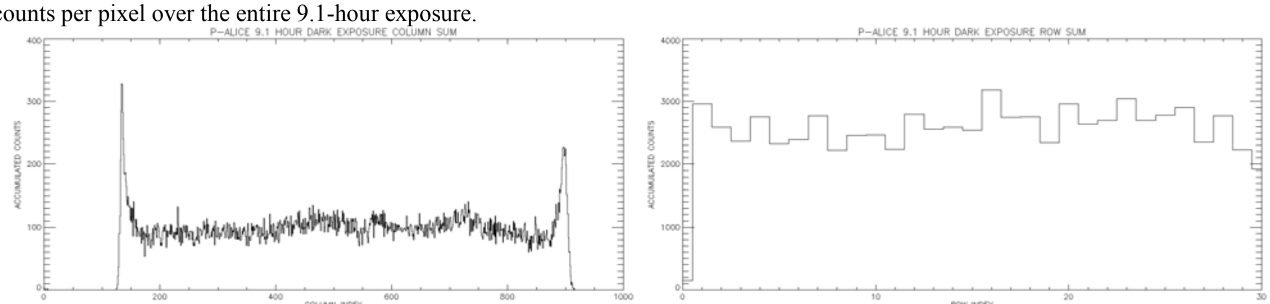

Figure 6. (Left) Column sum of the totaled 9.1-hours of dark exposure cal. Note the uniform distribution of events across the width of the detector active area. (Right) Row sum of the total 9.1-hour dark exposure. Note that a few rows (every third row to left and right of center) show slightly more output than expected with just pure spatially uniform noise characteristics (indicative of a pure Poissonian process). This periodic noise is a characteristic of the flat field performance of the detector and may be attributed to "DNL" noise in the analog-to-digital converters in the detector electronics.

3.2. Spatial/Spectral Resolution

3.2.1. Airglow Channel Point Spread Function

The spectral and spatial PSFs were measured with the airglow aperture at 0.5° intervals along the length of the slit and at specific wavelengths across the *P-ALICE* passband using argon and neon gasses in the hollow-cathode UV light

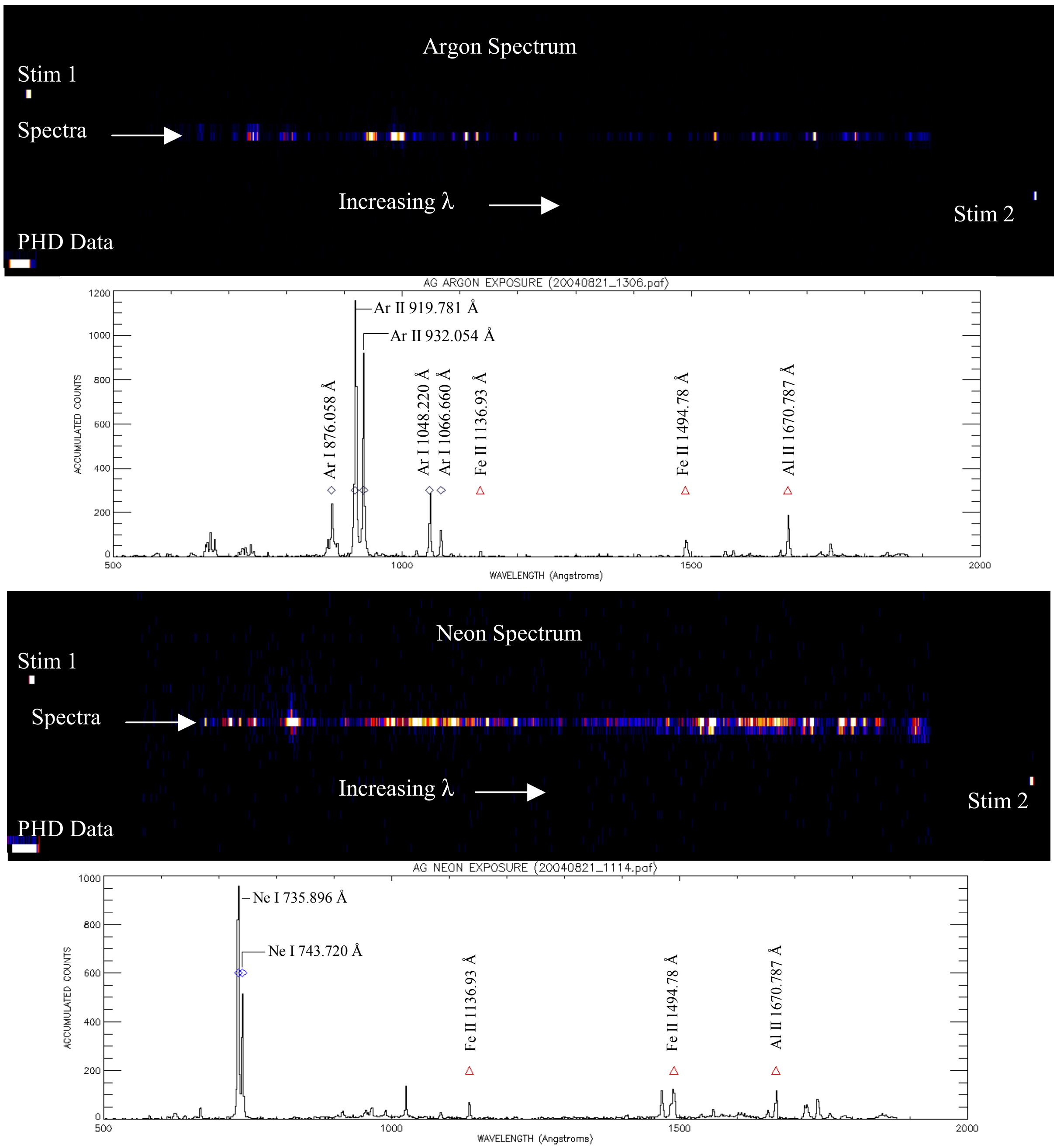

Figure 7. Histogram images and spectral plots of Ar (top) and Ne (bottom) spectra using a collimated point source input to the *P-ALICE* airglow channel at slit center. The pixel stims were powered on during the exposures. PHD data is also recorded and embedded in the histogram images. The blue diamonds show the emission lines from each noble gas. The red triangles are emission lines of iron and aluminum from the lamp cathode.

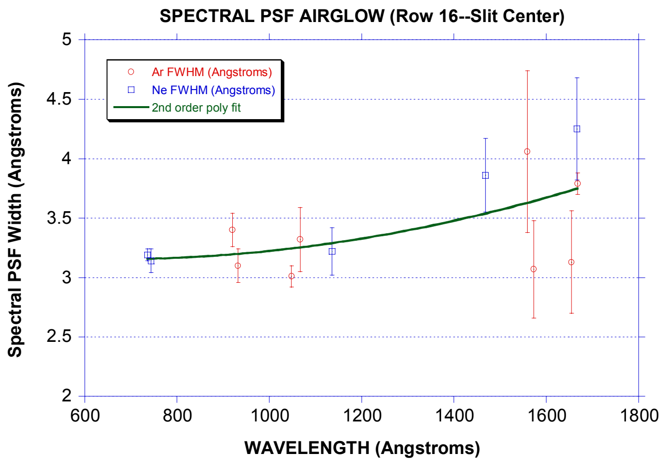

Figure 8. A plot of the measured spectral AG PSF as a function of wavelength at the center of the slit. The solid line is a 2nd order polynomial fit to the data. The error bars are one-sigma errors based on the Gaussian fits of the spectral profiles.

source. Point source images were acquired in histogram format at each slit location beginning at the center of the slit (spatial offset of 0°) and at offset angles of ±0.5°, ±1.0°, ±1.5°, ±2.0°, ±2.5°, and ±3.0° with respect to slit center. Figure 7 shows two histogram image exposures showing the recorded emission lines of Ar and Ne at slit center across the *P-ALICE* passband with the Acton monochromator set at zero order. The two stim pixels and the embedded pulse-height distribution data are also visible in the images.

For each exposure, the image row with the maximum number of counts was used to fit a series of Gaussians for each identified emission line in the spectral axis. In the spatial axis each column was fit with a Gaussian to determine the spatial PSF. Figure 8 shows the spectral PSF as a function of wavelength at slit center using the Ar and Ne exposures. The measured values varied between 3 and 4.5 Å, which satisfied the *P-ALICE* specification at slit center of < 6 Å FWHM. The measured spatial PSF across the *P-ALICE* passband was < 1.6 spatial pixels FWHM, satisfying the spatial PSF requirement of < 2 spatial pixels FWHM.

The spectral and spatial PSFs were found to slowly grow with off-axis angle along the length of the slit as expected. At the off-axis angles of ±2°, the spectral PSF varied between 4.4 and 6.5 Å FWHM, with an average of ~5 Å FWHM across the passband. The spatial PSF remained < 1.6 spatial pixels FWHM, but grew an average of ~0.2 spatial pixels from 0.6 to 0.8 spatial pixels FWHM, as the off axis angle was increased.

3.2.2. Airglow Channel Filled Slit Resolution

Filled slit images using a deuterium (D_2) lamp that flooded the airglow entrance aperture were acquired to determine the filled slit spectral resolution as well as the spatial plate scale. Figure 9 shows one such histogram image. A few discrete spectral emission lines exist about the H Ly-α emission at 1216 Å (i.e. emission lines are evident on either side of the photocathode gap), and a continuum of emission appears at the right side of the active area. The histogram clearly shows the image of the slit with the wide 2° x 2° SOC FOV at the top (the large square pattern) followed by the narrower 0.1° x 4° airglow FOV just underneath the SOC FOV (refer to the slit design in Fig. 3). In addition, the expected "slit curvature" aberration is clearly evident. This aberration was well characterized and implies that the wavelength scale offset is a function of the spatial location along the length of the slit.

One isolated emission line just to the left of the gap was used to compute an upper bound to the filled slit resolution. Figure 10 shows this emission at the center of the slit along with a Gaussian fit to it and its companion. The narrow emission has a FWHM spectral width of 9.0 ± 1.4 Å. This width is within the filled-slit resolution requirement of <18 Å FWHM for the airglow channel. The spatial plate scale was also derived from this data and was found to be 0.27° ± 0.01° per spatial pixel, which meets our < 0.3° per spatial pixel requirement.

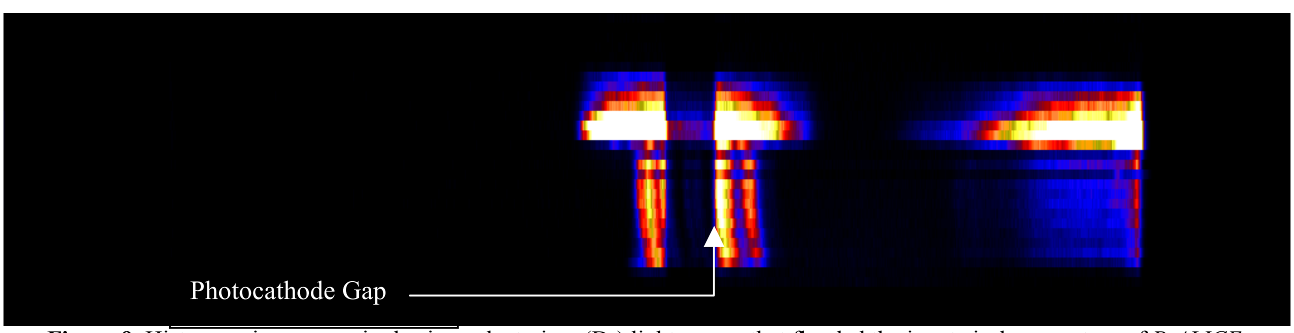

Figure 9. Histogram image acquired using a deuterium (D_2) light source that flooded the input airglow aperture of *P-ALICE*.

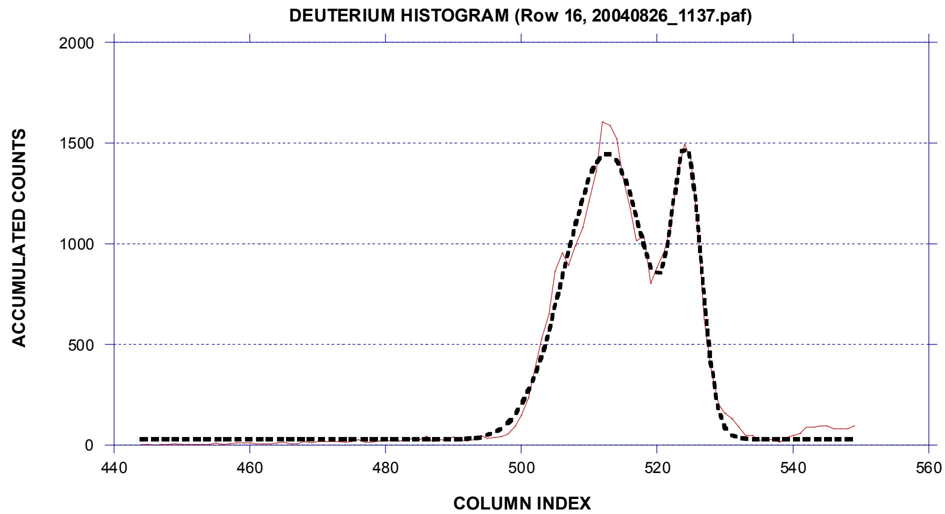

Figure 10. Plot of row 16 in the D_2 spectral image shown in Figure 9 (solid curve). A two Gaussian sum plus DC offset was fit to this profile (dashed line). The narrow emission on the right was used to calculate the filled slit spectral resolution.

3.2.3. Solar Occultation Channel Point Spread Function

The SOC spectral and spatial PSFs were measured at the center of the 2° x 2° slit SOC opening using argon (see Fig. 11) and neon gasses in the hollow-cathode UV light source. The image row with the maximum number of counts was used to fit a series of Gaussians for each identified emission line in these images. The measured spectral PSF as a function of wavelength varied between 2.7 and 3.5 Å FWHM (see Fig. 12) and thus easily meet our < 6 Å FWHM requirement.

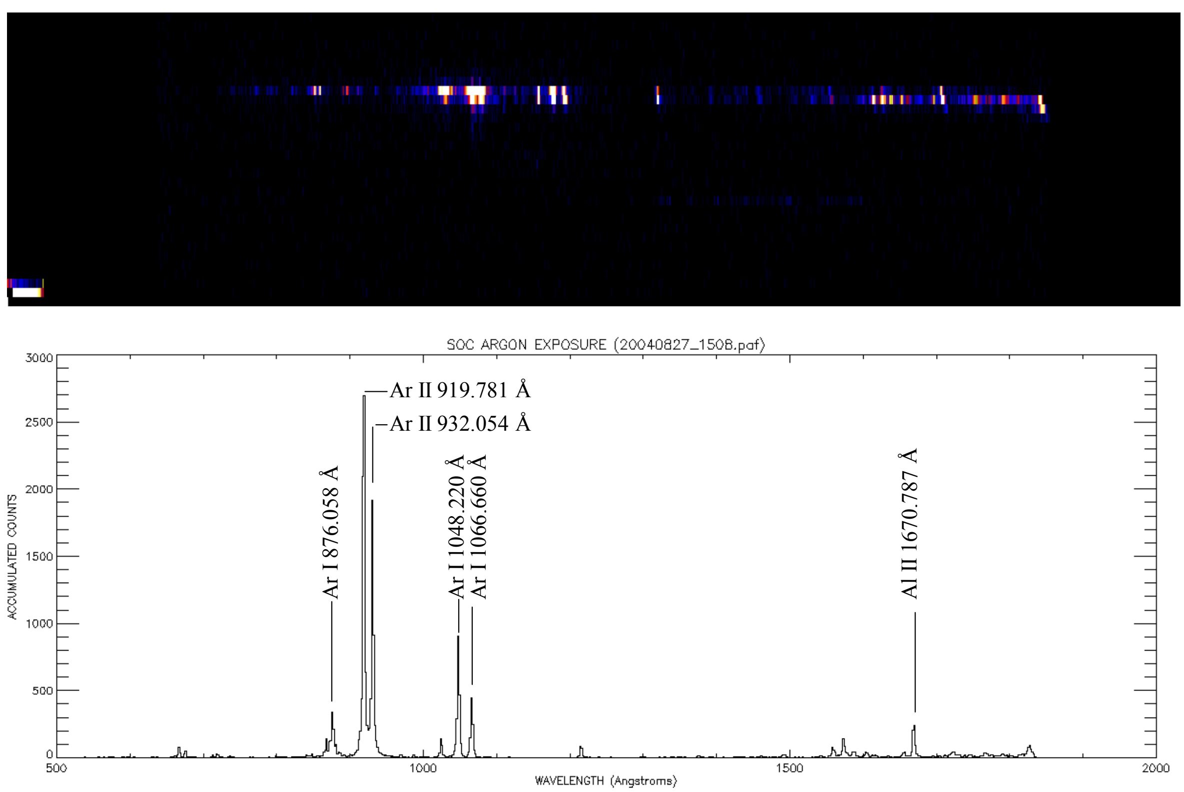

Figure 11. (Top) Histogram exposure of the argon spectrum through the SOC. (Bottom) Spectral profile of the above histogram image summed across rows 21-23.

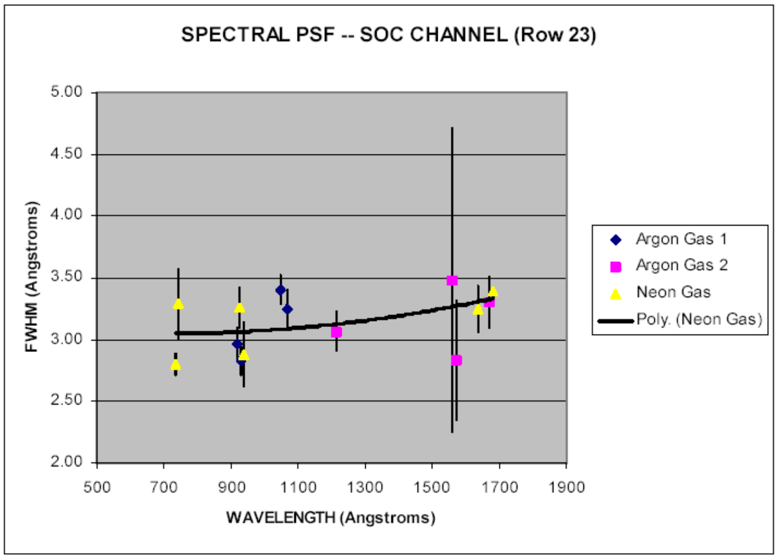

Figure 12. The measured spectral PSF at the center of the SOC FOV opening in the slit. The solid line is a 2nd order polynomial fit to the PSF data.

3.3. Wavelength Coverage/Calibration

The image histograms taken to determine the airglow PSF values were also used to determine the wavelength calibration at room temperature (+22ºC). Figure 13 shows the pixel locations of the four principal argon emission lines at 919.781, 932.054, 1048.22, and 1066.66 Å and the two bright neon emission lines at 735.896 and 743.72 Å at slit center. The spectral plate scale and linear offset were determined with a simple linear fit to this data: $d\lambda/dx = 1.815 \pm 0.004$ Å/pixel; offset (slit center) = 229.5 ± 1.5 Å (at pixel = 0). The linear fit is quite good—the χ^2 statistic for the fit is 1.93 with a linear correlation coefficient of 0.99999. The standard deviation of the wavelength residual between the linear fit and the six absolute emission line wavelengths is ±0.62 Å.

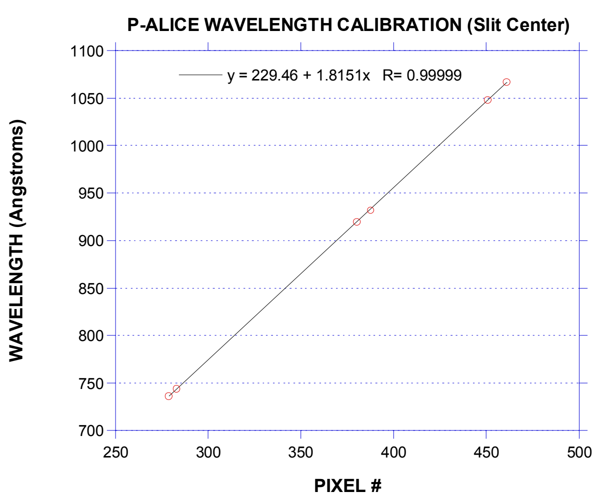

Figure 13. Plot of the measured positions of discrete Ar and Ne emissions versus wavelength at slit center. The solid curve shows the linear fit to the data to determine the spectral plate scale and offset. In the displayed equation, x represents the spectral pixel index (0 to 1023), and y represents wavelength in Ångstroms.

The total wavelength passband across the detector active area was computed with the above measured plate scale and offset values. The active area starts at spectral pixel 130 and ends at pixel 910. This area corresponds to a total wavelength passband of 465-1881 Å, which satisfies our minimal passband requirement of 520-1870 Å.

The wavelength offset varies slightly with the temperature of the detector electronics at a measured rate of ~0.1 pixels (deg C)$^{-1}$ towards longer wavelengths*. Therefore, care must be taken to apply the proper offset according to the detector electronics temperature. This temperature dependence was measured/calibrated during detector subsystem and instrument thermal vacuum testing. The wavelength offset also varies with the (x, y)-location of the point source image within the slit due to both instrument pointing and to slit curvature aberrations. Work is currently ongoing to determine these offset correction

* The wavelength offset value, therefore, shifts towards the blue at a rate of –0.2 Å (deg C)$^{-1}$. The plate scale variation with temperature is negligible and can be ignored.

terms and to establish a look-up table of correction values over the entire 465-1881 Å passband.

3.4. Scattered Light Characteristics

3.4.1. Off-Axis Light Scatter

The off-axis light scattering characteristics of the airglow channel were measured in both the horizontal and vertical axes of *P-ALICE*. Histogram images using a collimated input source and a vacuum UV hollow-cathode lamp gas mixture of H/He were acquired at angular input angles that varied between -8.9° and +9.2° with respect to the airglow boresight axis in the horizontal plane (perpendicular to the slit length with the vertical axis fixed at the center of the slit), and at input angles between -2.5° to +5.0° in the vertical plane (parallel to the slit length with the horizontal axis fixed at the center of the slit)[**].

The acquired histogram images were analyzed to determine the point source transmittance (PST) as a function of incident input angle to the *P-ALICE* boresight. The PST is defined as follows:

$$PST = \frac{E_{FP}}{E_{input}}, \tag{1}$$

where E_{FP} is the irradiance at the focal plane; and E_{input} is the input irradiance at the entrance aperture of the instrument. This expression can be written in terms of the measured off-axis angle count rate to the on-axis count rate ratio (R_{off}/R_0); the effective area averaged over the *P-ALICE* passband ($\overline{A_{eff}}$); the focal plane active area (A_{FP}); the average in-band QE of the detector photocathodes ($\overline{QE}$); and the ratio of the input beam area (A_{beam}) to the geometric area (A_g) of the AG entrance aperture (since the input beam under fills the entrance aperture). Notice that the PST is not normalized to unity at the zero degree offset position (on axis).

Using these parameters, Equation 1 becomes

$$PST = \left(\frac{\overline{A_{eff}}}{A_{FP}\,\overline{QE}}\right)\left(\frac{A_{beam}}{A_g}\right)\left(\frac{R_{off}}{R_0}\right). \tag{2}$$

The average effective area and QE values used in Equation 2 to compute the PST were values measured during instrument radiometric tests and detector QE tests at the detector vendor (Sensor Sciences, LLC), respectively: $\overline{A_{eff}}$ = 0.13 cm^2; $\overline{QE}$ = 0.27; A_{beam}/A_g = 0.05; A_{FP} = 7.5 cm^2. With these input values, Equation 2 gives a PST 0f 0.003 at an off-axis angle of zero degrees (i.e. on axis along the boresight with R_{off}/R_0 = 1).

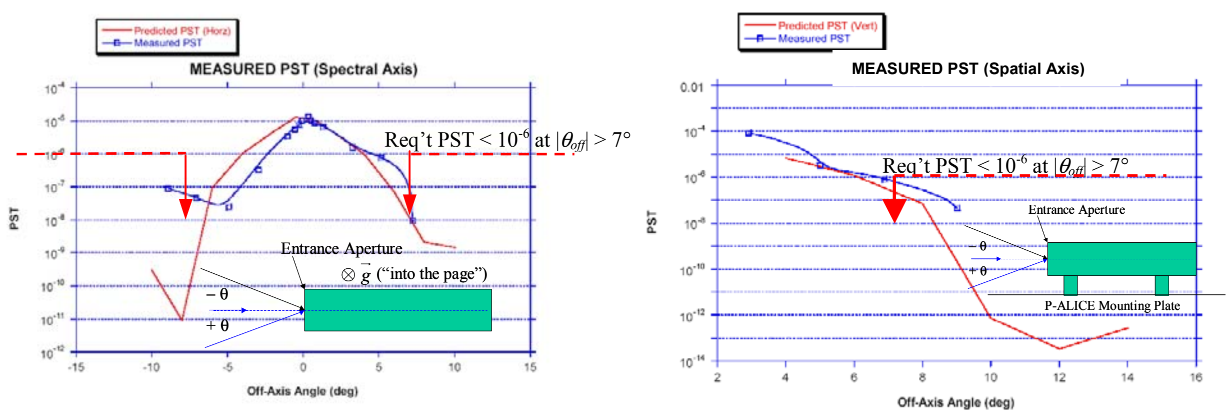

Figure 14. The measured PST as a function of the input off-axis angle with respect to the airglow boresight in the spectral axis (left) and spatial axis (right). Both the measured data values (blue squares) and the predicted PST (red solid curve based on the *P-ALICE* stray light analysis) are shown along with the specification requirement. The PST values near the 0 degree off-axis angle in the spectral axis are all outside the FOV of the slit in the horizontal axis (closest off-axis angle shown is at an off-axis angle of –0.07º where PST = 1.0 x 10^{-5}). The "inset" diagrams define the sign of the input offset angle.

[**] Volume constraints within the radiometric vacuum chamber limited the input offset angles to these values.

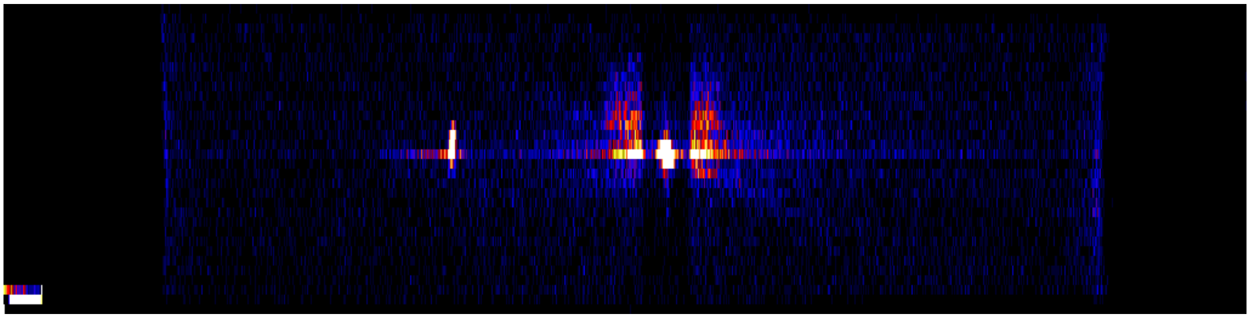

Figure 15. Histogram exposure of the H Ly-α emission. The primary emission is centered in the photocathode gap near the center of the active area; the wings of the emission and scattered light from the emission are evident outside the gap. The fainter emission to the left of center is the Ly-α ghost (see text).

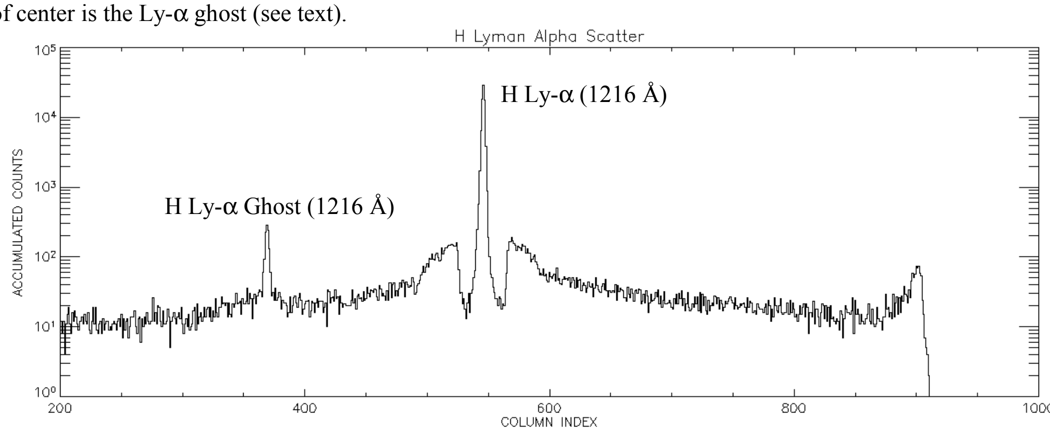

Figure 16. Spectral profile of the above histogram image showing the H Ly-α emission line centered in the PC gap and the Ly α ghost at 893 Å.

Figure 14 shows the measured PST as a function of off-axis angle in the spectral and spatial axes. Our requirement of a PST < 10^{-6} at off-axis angles > 7° was met in both axes. This requirement improves the viability of night-side observations of Pluto and Charon during the flyby.

3.4.2. H Ly-α Scatter

The total integrated scatter (TIS) at H Ly-α was measured using histogram exposures and a monochromatic collimated input light source at 1216 Å. This scatter is due primarily to imperfections in the grating surface. The TIS is defined as the ratio of detected counts outside the photocathode (PC) gap to the total counts within the emission line inside the gap (after the normalizing the inside rate with the ratio of the QE outside to inside the gap). This scatter can be expressed as follows:

$$TIS = \frac{R_o}{R_t}, \tag{3}$$

where R_o is the rate outside the PC gap; and R_t is the total normalized detector rate*. This ratio can be expressed in terms of the two measurable values r_t (the total detector rate) and r_i (the measured rate inside the gap). Equation 3 reduces to

$$TIS = \frac{r_t - r_i}{(k-1)r_i + r_t}, \tag{4}$$

where k is the ratio of the photocathode QE to that of the bare MCP glass inside the gap. Using the measured ratio of effective area just outside the PC gap to that inside the gap (this ratio is nearly equivalent to the ratio of QE values), we find that k = 9.2. Inserting the above values into Equation 4 gives a TIS for H Ly-α of 0.024 (2.4%). This result is well within the TIS goal of <10%.

---

* These detector rates have been corrected for electronic deadtime effects.

Figures 15 and 16 show, respectively, the 300-second histogram exposure and spectral profile taken to make this measurement. The H Ly α emission line within the PC gap is evident along with the wings of the emission line protruding on either side of the PC gap as well as light scatter across the active area. In addition, a ghost image of the Ly α line shows up left of center in the image. This ghost was also noted in the *R-ALICE* instrument. Ray trace studies of *P-ALICE* show that this ghost is caused by the reflection of the H Ly α emission line off the front surface of the detector MCP back towards the grating, which then re-diffracts the light back onto the detector surface. The intensity of this ghost is nearly identical to that measured with *R-ALICE*.

3.5. Absolute Effective Area

3.5.1. Airglow Channel

The effective area of the airglow channel was measured across the *P-ALICE* passband at discrete wavelengths using emission lines from neon, argon, and a hydrogen/helium gas mix covering a wavelength range of 584 – 1603 Å. Histogram exposures were made with the chamber's monochromator set to the specific measurement wavelength. The monochromator output slit was set to provide a detector output count rate that did not show any saturation effects in the pulse-height distribution (i.e. too high a local flux on the MCP stack will cause a local gain drop that is evident in the PHD data). Background exposures were also taken for each illuminated exposure to allow for dark subtraction.

The beam flux was measured for each effective area measurement using a NIST calibrated silicon (Si) photodiode. In most cases, the beam flux had to be increased in intensity to allow enough flux for a measurement with the photodiode. However, this increased level flux was too high for a measurement with *P-ALICE* causing local MCP saturation. An Amptektron channeltron was used to measure the ratio of the beam fluxes at both the low and high intensity levels that provided a correction factor to the flux measured by the NIST photodiode.

Figure 17 shows the measured effective area as a function of wavelength λ, $A_{eff}(\lambda)$. The equation used to compute A_{eff} is

$$A_{eff}(\lambda) = \frac{A_g R(\lambda)}{\Phi(\lambda)}, \quad (5)$$

where A_g is the geometric area of the *P-ALICE* airglow entrance aperture (16 cm^2); $R(\lambda)$ is the detector count rate (corrected for the detector deadtime and the detector background), and $\Phi(\lambda)$ is the input flux to the instrument based on measurements with the NIST Si photodiode and the channeltron. The red circles in the figure show the measured effective area values; the green squares show the predicted values based on reflectivity values of the OAP mirror and grating (including the grating diffraction efficiency), and the photocathode QE response measured during subsystem level optics and detector tests. The blue solid line (no data points) is the minimum effective area requirement set for the instrument. As is evident in Figure 17, the effective area requirement was met with significant margin.

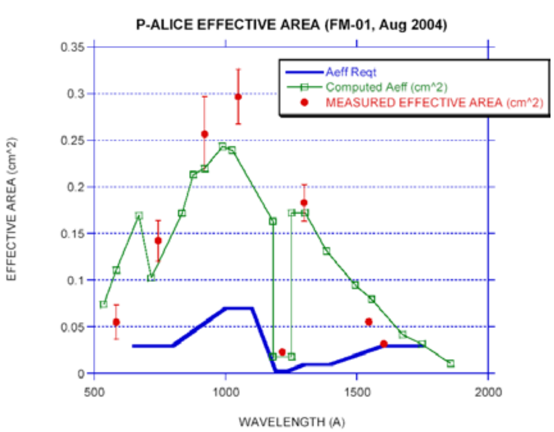

Figure 17. The measured effective area for the airglow channel (red solid circles) plotted versus wavelength. Also shown are the computed effective area values (green open squares) based on previously measured SiC reflectivity values of the OAP mirror and grating and detector QE values. The instrument effective area requirement is shown as the solid blue line in the lower portion of the graph.

3.5.2. Solar Occultation Channel

The effective area of the SOC was measured, and the relative sensitivity compared with the AG channel was computed. Figure 18 shows the measured ratio of effective area between the AG and the SOC along with the predicted ratio based on the measured SiC-coated SOC relay mirror and the ratio of entrance aperture areas. Note that the AG channel is 3000-7300 (wavelength dependant) times more sensitive that the SOC channel, with an average ratio of ~5000.

The ratio of AG to SOC effective area requirement is set to limit the detector count rate to < 30 kHz during the solar occultation observations at Pluto/Charon. This ratio must be >2400 to meet this requirement; as we see above, this requirement was easily met.

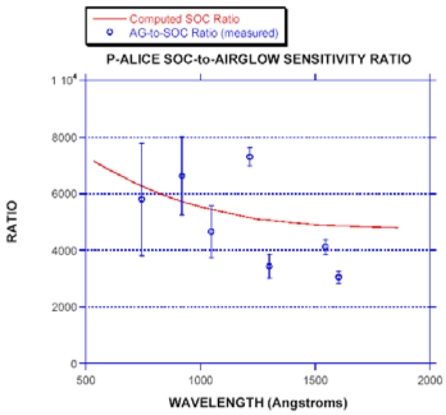

Figure 18. The measured relative sensitivity of the SOC (normalized to the airglow channel) versus wavelength. The red curve is the calculated ratio.

4. CONCLUSIONS

The *P-ALICE* flight unit has successfully completed all environmental and radiometric tests; it was successfully delivered and integrated to the *New Horizons* spacecraft in September 2004. The instrument has been working flawlessly throughout the spacecraft integration and test activities. The demonstrated radiometric performance described herein indicates that *P-ALICE* will meet all the scientific objectives proposed for its mission aboard *New Horizons*, which is planned for launch in January 2006.

An extensive in-flight radiometric characterization and calibration is planned for *P-ALICE* during the early phases of the mission to characterize its in-flight performance. Hot UV stars as well as the Sun and Jupiter will be observed with *P-ALICE* to make this in-flight calibration. These data along with ground calibration results will provide the necessary database required to calibrate *P-ALICE* data taken during the mission.

ACKNOWLEDGEMENTS

We wish to thank the entire *P-ALICE* engineering and support team at SwRI, with special thanks to John Stone, Maarten Versteeg, Greg Dirks, and Kristian Persson. We also wish to thank Oswald Siegmund, John Vallerga, and Rick Raffanti of Sensor Sciences, LLC for their invaluable contribution to the development and testing of the *P-ALICE* DDL detector subsystem. This work was supported by NASA contract #NASW02008.

REFERENCES

1. Stern, S. Alan, David C. Slater, William Gibson, Harold J. Reitsema, Alan Delamere, Donald E. Jennings, Dennis C. Reuter, John T. Clarke, Carolyn C. Porco, Eugene M. Shoemaker, and John R. Spencer, “The Highly Integrated Pluto Payload System (HIPPS): A Sciencecraft Instrument for the Pluto Mission,” in *EUV, X-Ray, and Gamma-Ray Instrumentation for Astronomy VI*, Proceedings of SPIE Vol. **2518**, O.H.W. Siegmund and John Vallerga, Editors, 39-58 (1995).
2. Slater, D. C., S. A. Stern, T. Booker, J. Scherrer, M. F. A'Hearn, J. L. Bertaux, P. D. Feldman, M. C. Festou, and O. H. W. Siegmund, “Radiometric and calibration performance results for the Rosetta UV imaging spectrometer *ALICE*,” in *UV/EUV and Visible Space Instrumentation for Astronomy and Solar Physics*, Oswald H. W. Siegmund, Silvano Fineschi, Mark A. Gummin, Editors, Proceedings of SPIE Vol. **4498**, 239-247 (2001).
3. Stern, S. A., J. Scherrer, D. C. Slater, G. R. Gladstone, L. A. Young, G. Dirks, J. Stone, M. Davis, and O. H. W. Siegmund, “*ALICE*: The ultraviolet imaging spectrograph aboard the *New Horizons* spacecraft,” in *X-Ray, UV, Visible, and IR Instrumentation for Planetary Missions*, Oswald H. W. Siegmund and G. Randall Gladstone, Editors, Proceedings of SPIE Vol. **5906B**, (2005).
4. Siegmund, O. H. W., J. Stock, R. Raffanti, D. Marsh, and M. Lampton, “Planar Delay Line Readouts for High Resolution Astronomical EUV/UV Spectroscopy,” in *UV and X-Ray Spectroscopy of Astrophysical and Laboratory Plasmas*, Proceedings from the 10th International Colloquium, Berkeley, CA 3-5 February 1992, 383-386 (1992).
5. Siegmund, O. H. W., “Microchannel Plate Imaging Detector Technologies for UV Instruments,” in Conference Proceedings *From X-rays to X-band—Space Astrophysics Detectors and Detector Technologies*, Space Telescope Science Institute, (2000).
6. Danzmann, K., M. Günther, J. Fischer, M. Kock, and M. Kühne, “High current hollow cathode as a radiometric transfer standard source for the extreme vacuum ultraviolet,” *Applied Optics*, **27**, 4947-4951 (1988).